


# On-Chip Detection of Electronuclear Transitions in the $^{155,157}\text{Gd}$ Multilevel Spin System

G. Franco-Rivera<sup>1,\*</sup>, J. Cochran<sup>1</sup>, L. Chen<sup>2</sup>, S. Bertaina<sup>3</sup>, and I. Chiorescu<sup>1,†</sup>

<sup>1</sup>*Department of Physics and National High Magnetic Field Laboratory, Florida State University, Tallahassee, Florida 32310, USA*

<sup>2</sup>*Center for Excellence in Superconducting Electronics, Shanghai Institute of Microsystems and Information Technology, Chinese Academy of Science, Shanghai, China*

<sup>3</sup>*CNRS, Aix-Marseille Université, IM2NP (UMR 7334), Institut Matériaux Microélectronique et Nanosciences de Provence, Marseille, France*

 (Received 1 October 2021; revised 27 January 2022; accepted 22 June 2022; published 21 July 2022)

The properties of rare-earth elements diluted in nonmagnetic crystals make them promising candidates for a quantum memory due to their limited Hilbert space. The control and readout of the qubit states require a highly sensitive measurement and large coupling of the spin ensemble with the electromagnetic mode of a superconducting resonator. We report sensitive detection of forbidden transitions of electronuclear states from the minority species of  $^{155}\text{Gd}$  and  $^{157}\text{Gd}$  isotopes, which opens the possibility of connecting quantum states with very different spin projections. Cavity perturbation measurements seen in the reflected signal allow the detection of about  $7.6 \times 10^7$  spins and the measurement of phase memory loss rate and spin-photon coupling strength.

DOI: [10.1103/PhysRevApplied.18.014054](https://doi.org/10.1103/PhysRevApplied.18.014054)

## I. INTRODUCTION

The implementation of quantum information processors can benefit from the use of hybrid quantum systems that harness the strengths of multiple qubit platforms. On the one hand, superconducting qubits have fast logic-gate operations with high fidelity, while their performance is limited by the qubit decoherence times [1]. To circumvent this problem, hybrid systems combine superconducting circuits with other two-level systems (TLS) acting as a memory to store and retrieve the quantum information. Among the TLS, spin qubits are proposed as quantum memories given their long decoherence and relaxation times [2,3]. Such systems exploit the electron or nuclear spin degree of freedom, which can be coupled to resonant electromagnetic modes in superconducting or three-dimensional cavities [4], acting as a bus between the superconducting qubit and the spin ensemble [5].

Many spin-ensemble-based systems have been investigated as prospects for storing quantum information, including organic radical magnets [6–8], N-V centers in diamond and other point defects in Si [9–13], and quantum spins in crystals [14–20]. Recent studies using  $\text{Er}^{3+}:\text{Y}_2\text{SiO}_5$  spin-diluted crystals [21], N-V centers in diamond [22], and Bi defects in Si [23] demonstrated storing

and retrieving the state of microwave photons at high power and near the quantum limit regime.

Incorporating rare-earth (RE) ions in nonmagnetic matrices has generated considerable interest as potential candidates as well [14–16,24–28]. In particular, the *S*-state lanthanides ( $\text{Eu}^{2+}$ ,  $\text{Gd}^{3+}$ ,  $\text{Tb}^{4+}$ ) have zero total orbital angular momentum, which partially suppresses the spin-lattice and crystal-field interactions [29]. These large-spin ( $S = 7/2$ ) ions possess a rich energy-level structure that spans the Hilbert space of a three-qubit system allowing a quantum gate to be obtained by applying resonant  $\pi$  pulses [17,30].

In the present report we study electronuclear transitions at the mesoscale level of the minority species of  $^{155}\text{Gd}^{3+}$  and  $^{157}\text{Gd}^{3+}$  ( $I = 3/2$ ) isotopes, in order to achieve local (on-chip) control of the electronic and nuclear degrees of freedom. In the Gd odd isotopes, the nonzero *I* creates  $2I + 1$  hyperfine split electronuclear states with transition frequencies close enough to be studied with the single mode of an on-chip resonator by means of field tuning of the resonance frequency [31]. The  $\text{Gd}^{3+}$  ions are diluted in a  $\text{CaWO}_4$  single crystal and weakly coupled with the electromagnetic mode of a coplanar stripline superconducting resonator. The  $\text{CaWO}_4$  host matrix provides a large crystal field that gives spin transitions at approximately 18 GHz. The microwave field distribution induced by the resonator geometry allows us to connect electronuclear quantum states with very different spin projections

\*[gfranco@magnet.fsu.edu](mailto:gfranco@magnet.fsu.edu)

†[ic@magnet.fsu.edu](mailto:ic@magnet.fsu.edu)

( $\Delta m_s \neq 1$ ) that would otherwise be forbidden. The large values for the spin of a RE ion, cavity resonant frequency, and spin projection swing contribute to an increase of the overall spin-photon coupling strength. This makes the  $^{155,157}\text{Gd}^{3+}:\text{CaWO}_4$  spin crystal an interesting candidate for a quantum hybrid system when integrated into current circuit quantum electrodynamics architectures.

## II. RESONATOR DESIGN AND EXPERIMENTAL SETUP

The on-chip microwave resonators are built from a 20-nm Nb thin film deposited in a Si/SiO<sub>2</sub> substrate (300 nm of SiO<sub>2</sub>) using dc magnetron sputtering. For the resonator pattern standard UV lithography techniques and reactive ion etching in a CF<sub>4</sub>-O<sub>2</sub> atmosphere are used to obtain the desired structure. The use of such thin films allows one to apply in-plane magnetic fields without considerably modifying the resonator quality factor  $Q$ , due to field-induced losses [31–33]. The resonator geometry has a designed transition from a coplanar waveguide to a coplanar stripline [34] with all dimensional parameters corresponding to a 50- $\Omega$  impedance. A  $\lambda/4$  resonator is realized by interrupting the stripline thus creating a capacitive coupling between the resonator and the transmission line. At the end of the resonator, a short-circuit termination is designed to have an  $\Omega$  shape with internal radius of 15  $\mu\text{m}$  [see Fig. 1(a)]. The microwave energy, and in particular its magnetic field component, is concentrated in this  $\Omega$  loop and the Gd sample is to be placed directly on top.

The resulting resonator and the sample holder are thermally anchored to the mixing chamber of a dilution refrigerator via a cold finger that centers the sample inside a large superconducting vector magnet. The temperature at the sample stage is kept at  $T \simeq 0.38$  K. A schematic diagram of the full measurement setup is presented in Fig. 1(b). A long microwave (MW) pulse of 25  $\mu\text{s}$  is sent by a synthesizer to probe the cavity-spin system. The signal is attenuated at different stages of the dilution refrigerator to reduce the thermal noise coming from room temperature. At the sample holder stage, the signal passes through a circulator allowing isolation of the reflected signal towards the output line. To excite different electronuclear transitions, a superconducting vector magnet is used allowing precise tuning of the in-plane field with a 0.2-G resolution. The reflected signal is amplified at room temperature by 35 dB in the range 17–20 GHz before being down-mixed with a lower-frequency tone (LO). A band-pass filter centered at  $\omega_{\text{rf}} - \omega_{\text{LO}}$  is used before further amplification. The signal is finally recorded and digitized by a high-speed acquisition card.

We can estimate the volume of the microwave magnetic field using COMSOL MULTIPHYSICS finite-element (FE) simulations. Evaluations of  $H_1$  are shown in Fig. 2(a)

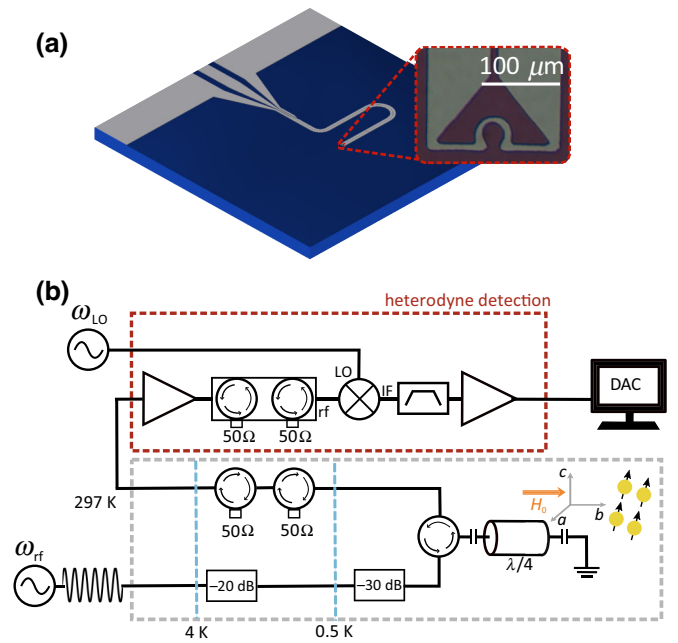


FIG. 1. (a) Coplanar stripline resonator design; the inset shows a photograph of the  $\Omega$ -shaped termination. (b) Heterodyne detection schematics. An excitation pulse is generated by means of a MW synthesizer. The signal is attenuated at the different stages of a dilution refrigerator before reaching the on-chip resonator anchored at  $T \simeq 0.38$  K. The reflected signal is then amplified at room temperature before down-mixing by a lower tone signal and as recorded by a Digital-to-Analog Converter (DAC)

for a cut through the center of the  $\Omega$ -shaped termination and at the chip surface [Fig. 2(b)]. Using the full chip geometry, one can identify the volume  $V_m$  containing  $H_1$  field ranging from the maximum value  $H_1^{\text{max}}$  near the surface to a certain threshold  $H_{\text{th}}$  as shown in Fig. 2(c) as a function of  $H_{\text{th}}/H_1^{\text{max}}$ . Following the definition of a mode volume [35,36],  $(\int H_1^2 dV)^2 / \int H_1^4 dV$ , one can get an approximate value using the equation

$$V_m = \frac{\left(\int_{V_{\text{sample}}} H_1^2 dV\right)^2}{\int_{V_{\text{cavity}}} H_1^4 dV}, \quad (1)$$

where  $V_{\text{sample}}$  and  $V_{\text{cavity}}$  are the sample and full chip volumes, respectively. One obtains a mode volume of about 1100  $\mu\text{m}^3$ , similar to the value at  $H_{\text{th}}/H_1^{\text{max}} = 0.3$ . Further away from this threshold, the magnetic energy density drops to approximately 5% of that near the  $\Omega$  loop.

## III. FIELD-DEPENDENT SPECTROSCOPIC MEASUREMENTS

A single crystal of  $\text{Gd}^{3+}:\text{CaWO}_4$  with a 0.05% spin concentration is placed on top of the  $\Omega$  loop of the Nb resonator and the setup described above is used to record the

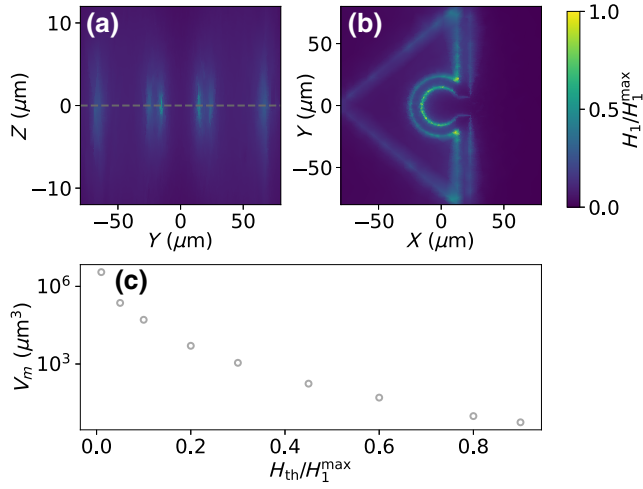


FIG. 2. (a) FE simulation of the normalized  $H_1$  field distribution at the center of the  $\Omega$ -shaped loop shows the field intensity drops by 70% above  $3 \mu\text{m}$  of the chip surface ( $Z = 0 \mu\text{m}$ ). (b) Top view of the  $\Omega$ -shaped termination at the chip surface showing where the MW  $H_1$  field is concentrated. (c) Volume calculation versus  $H_{\text{th}}/H_{\text{max}}$ ; a mode volume of  $1100 \mu\text{m}^3$  is obtained in agreement with an estimation using Eq. (1).

reflected signal as a function of field and frequency. At resonance, the microwave frequency  $\omega$  matches the spin-level splitting and the absorbed power generates a dip in the reflected signal. The electronuclear levels are eigenvalues of the  $\text{Gd}^{3+}$   $S = 7/2$  ion in the  $I4/a$  tetragonal symmetry [38] of the host matrix [39]:

$$\mathcal{H} = \mu_B \mathbf{H}_0^T \mathbf{g} \mathbf{S} + \mathbf{S}^T \mathbf{A} \mathbf{I} + B_2^0 O_2^0 + B_4^0 O_4^0 + B_4^4 O_4^4 + B_6^0 O_6^0 + B_6^4 O_6^4, \quad (2)$$

where  $O_p^k$  are the Stevens operators [40],  $\mu_B$  is the Bohr magneton,  $\mathbf{H}_0$  is the applied magnetic field vector, and  $(g_{\parallel}, g_{\perp}) = (1.991, 1.992)$  are the  $g$ -factors parallel and perpendicular to the crystallographic  $c$  axis, respectively. The presence of the  $^{155}\text{Gd}$  ( $A_{155} = 12.40$  MHz abundance 14.7%) and  $^{157}\text{Gd}$  ( $A_{157} = 16.28$  MHz abundance 15.7%) [29,39] isotopes with nuclear spin  $I = 3/2$  causes the splitting of each electronic  $^8S_{7/2}$  multiplet into  $2I + 1$  states. As discussed below, our spectroscopically found values for the prefactors of the Stevens operators are within an approximately 2% difference of values obtained in previous studies [41].  $\mathbf{H}_0$  provides an *in situ* tool to control the admixture of states of different  $S_z$  projections. In the present study, the field is applied almost perpendicular to the  $c$  axis, as discussed below, leading to a significant mixture of pure  $|S_z\rangle$  states. Some of the eigenstates are shown in the Supplemental Material [37].

Measurements of the reflected microwave power as a function of frequency and magnetic field are given in Fig. 3(a); for a fixed field, the excitation signal is swept around the cavity resonance and the process is repeated

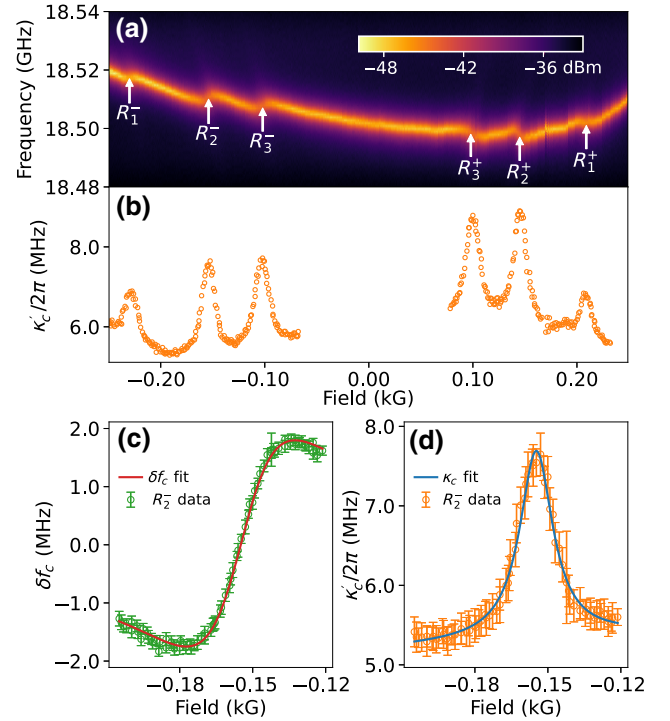


FIG. 3. (a) Field-dependent cavity spectroscopy signal. Interactions between the spins and the cavity mode are highlighted by the white arrows. (b) Measured field-dependent cavity width,  $\kappa'_c$ , across each resonance. The cavity width is obtained from fitting the reflection amplitude parameter  $S_{11}$  to the frequency sweep cross section of the contour scan (see Ref. [37]). (c) Measured cavity resonance frequency perturbation  $\delta f_c$  and (d) cavity widths  $\kappa'_c$  for the spin transition labeled  $R_2^-$  represented by the navy and red circles, respectively. Fits to the measured resonance frequency and cavity width perturbation are performed using Eqs. (3) and (4).

from negative to positive values of the magnetic field. The contour plot identifies six spin resonances visible as a perturbation of the cavity resonance frequency. As a side note, one observes that the field dependence of the cavity resonance is not a quadratic decrease with field [31,42]. This could be due to how the main nuclear  $\text{Gd}^{3+}$  species,  $I = 0$ , couples with the cavity; classically, the sample magnetization in field can change the resonator inductance. Nevertheless, this aspect is of secondary importance to the current study, which focuses on the electronuclear transitions of the minority species  $I = 3/2$ .

The perturbation of the cavity properties by a spin transition is significant in the case of superconducting planar cavities, due to a reduced mode volume, leading to a large filling factor. In the limit of weak spin-photon coupling, the effect of dissipation can be represented by using a complex frequency  $\bar{\omega}_c = \omega_c - i(\omega_c/2Q) = \omega_c - i\kappa_c$ . By introducing a magnetic sample in the cavity, the resonator inductance changes and the complex resonance frequency becomes  $\delta\bar{\omega}_c = \delta\omega_c - i\delta\kappa_c$ . The relative shift in frequency

is proportional to the sample's susceptibility  $\delta\bar{\omega}_c/\omega_c = -\beta\bar{\chi} = -\beta(\chi' - i\chi'')$ ,  $\beta$  being a geometric factor that depends on the spin distribution around the resonator volume and its coupling to the cavity mode [14,43]. By analyzing the real and imaginary part of the expression, one can find the dependence on frequency. It is important to note that even in the weak coupling regime, large filling and  $\beta$  factors can lead to perturbations so large that the  $Q$  factor becomes impossible to measure.

In a similar way, the following expressions derived from the input-output formalism in the presence of a spin system [44] describe the perturbation of the cavity resonance and width:

$$\omega'_c = \omega_c + \frac{g_c^2 \Delta}{\Delta^2 + \gamma_s^2}, \quad (3)$$

$$\kappa'_c = \kappa_c + \frac{g_c^2 \gamma_s}{\Delta^2 + \gamma_s^2}, \quad (4)$$

where  $\omega_c$  and  $\kappa_c$  are the unperturbed cavity resonance frequency and width, respectively,  $\gamma_s$  is the spin's phase memory loss rate,  $g_c$  is the cavity spin-ensemble coupling constant, and detuning  $\Delta = \omega - \omega_s$  is defined as the difference between the probing frequency  $\omega$  and the level separation  $\omega_s$  between the two electronuclear levels under investigation. Consequently, the power reflected by the cavity can be written as (see also Refs. [45,46])

$$|S_{11}|^2 = \left| 1 + \frac{\kappa_e}{i(\omega - \omega'_c) - \kappa'_c} \right|^2, \quad (5)$$

where  $\kappa_e$  is the dissipation due to external factors and in practice is approximately equal to  $\kappa_c$  or  $\kappa'_c$ . Equation (5) can reproduce a double-dip  $\omega$  scan characteristic of the strong-coupling regime for a cooperative factor  $C = g_c^2/\kappa_c\gamma_s \gtrsim 1$ . For  $C \ll 1$ ,  $|S_{11}(\omega)|^2$  has a Lorentzian behavior with a perturbed center and width, as in this study.

The reflected power measurements presented in Fig. 3(a) are fitted with Eq. (5) for each field. Details of the fitting procedure and a representative example are provided in the Supplemental Material [37]. The process is repeated for each field and the obtained dependence of  $\kappa'_c/2\pi$  on field is shown in Fig. 3(b). Similarly, the field dependence of the perturbed  $\omega'_c/2\pi$  is obtained. To extract the values of the  $g_c/2\pi$  and  $\gamma_s/2\pi$  parameters, fits using Eqs. (3) and (4) as a function of detuning  $\Delta$  are needed. As detailed in the Supplemental Material [37], numerical diagonalization of the spin Hamiltonian is required to establish the relationship between  $\omega_s$  and the applied field. This is particularly of essence in the case studied here, where the static field is applied perpendicularly to the  $c$  axis to give a finite probability to transitions otherwise considered forbidden. Note that while  $\Delta$  is controlled by magnetic field, the perturbation analysis provides  $\gamma_s/2\pi$  and  $g_c/2\pi$  in hertz. Examples

of fits using Eqs. (3) and (4) (to which a linear background is added; see Supplemental Material for details) are shown in Figs. 3(c) and 3(d).

The field dependence of  $\omega_s$  for each studied resonance is found using the EasySpin package [47]. A single value of  $A = 14.34$  MHz is used for simplicity since the field separation between odd-isotope resonances lies well within the resolution of our spectroscopic measurements. The crystal field parameters  $B_2^0 = -938.4$ ,  $B_4^0 = -1.247$ ,  $B_4^4 = -7.305$ ,  $B_6^0 = 5.712 \times 10^{-4}$ , and  $B_6^4 = 70.0 \times 10^{-4}$  (all in MHz) are determined by least-squares comparison between the experimental resonance fields and fields obtained from numerical diagonalization of the spin Hamiltonian.

The obtained eigenvalues of  $\mathcal{H}$  are presented in Fig. 4 for applied fields parallel (navy) and close-to-perpendicular (dark red) to the  $c$  axis. For parallel  $\mathbf{H}_0$  fields the calculated eigenvalues are characterized by good quantum numbers  $S_z$  and split by the crystal field for  $\mathbf{H}_0 = 0$ . A static field almost perpendicular to the easy axis ( $\beta \sim 90^\circ$  and fine tuned in EasySpin) causes an admixture of the  $S_z$  states between the electronic multiplet ground state and its third excited state, causing a swing in spin projection of approximately 4–5 while  $\Delta I_z = 0$  (see Supplemental

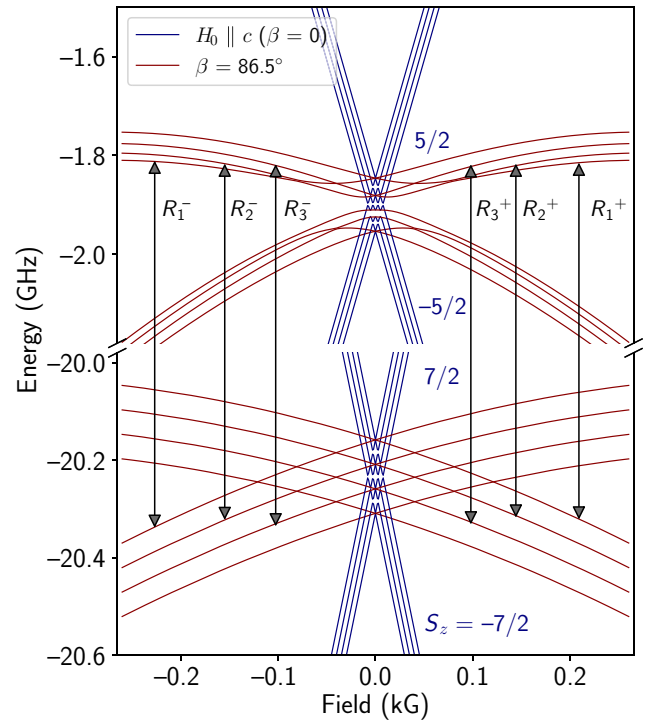


FIG. 4. Energy levels of the  $\text{Gd}^{3+}$  spin Hamiltonian obtained from diagonalization for fields applied parallel (navy,  $\beta = 0^\circ$ ) and close-to-perpendicular (dark red,  $\beta = 86.5^\circ$ ) to the crystallographic  $c$  axis. The observed transitions are shown by arrows and arise from the hyperfine splitting ( $\Delta I_z = 0$ ) of the ground and third excited state of the  ${}^7/2S_8$  electronic multiplet.



Material [37] for tabulated values). The aforementioned transitions are highly forbidden in the context of conventional ESR where  $\Delta S_z = 1$ . The observed resonances are highlighted in Fig. 4 with gray arrows. Only the three highest-probability transitions of the  $2I + 1$  hyperfine resonances are observed as can be seen in the field-dependent spectroscopic measurements of Fig. 3.

#### IV. DECOHERENCE RATES AND SPIN SENSITIVITY

From the fits of the six resonances, similar to those shown in Figs. 3(c) and 3(d), the  $\gamma_s$  rate and the cavity-spin-ensemble coupling strength  $g_c$  are obtained. The values are listed in Table I in increasing order of the field derivative  $|\partial\omega_s/\partial H_0|_r$  of  $\omega_s$  at resonance  $\Delta = 0$ . In the case of the linewidth fit [Eq. (4)], its peak is located over a narrower region of the field and therefore the fit reliability is less sensitive to background variations. In contrast, the  $\omega'_c$  function covers a large field span around a resonance and can be affected by the nonlinear background of  $\omega_c(H_0)$ . The values of  $\gamma_s$  obtained from the  $\kappa'_c$  fit are shown in Fig. 5 as a function of the field derivative, where  $|\partial\omega_s/\partial H_0|_r$  is given in units of  $\gamma_e/2\pi = 2.8025$  MHz/G, the gyromagnetic ratio of the free electron. The positive correlation between decoherence rate and slope agrees with the known view that decoherence is improved when field noise is canceled in first order (so-called clock transitions). The rates  $\gamma_s$  obtained from the resonance frequency perturbation are fluctuating around a weighted average value of  $12.2 \pm 1.6$  MHz but are likely to be more affected by systematic errors as mentioned above. Other fit parameters are the unperturbed cavity resonance  $\omega_c$ , which follows the nonlinear background (see Fig. 3), and the unperturbed cavity width  $\kappa_c$ . The latter gives an average value  $\kappa_c/2\pi = 5.84 \pm 0.13$  MHz leading to a cooperativity factor  $C$  with an overall range from 0.15 to about 0.45.

TABLE I. Spin decoherence rate  $\gamma_s$  and spin-photon effective coupling constant  $g_c$  for each of the six transitions [labels as in Fig. 3(a)] from perturbed cavity width and resonance frequency fits. The nuclear quantum number  $I_z$  of levels involved in the transition is given as well.

$I_z$	$\gamma_s/2\pi$ (MHz)		$g_c/2\pi$	
	Cavity width	Frequency shift	$\gamma_s/2\pi$ (MHz)	$g_c/2\pi$
$R_1^-$	$7.3 \pm 0.4$	$3.0 \pm 0.1$	$11.0 \pm 0.6$	$3.3 \pm 0.1$
$R_1^+$	$7.6 \pm 0.5$	$2.9 \pm 0.1$	$9.4 \pm 2.2$	$2.7 \pm 0.2$
$R_2^-$	$8.1 \pm 0.25$	$4.4 \pm 0.1$	$19.9 \pm 0.25$	$8.0 \pm 0.1$
$R_2^+$	$9.0 \pm 0.4$	$5.0 \pm 0.1$	$10.2 \pm 0.5$	$5.2 \pm 0.1$
$R_3^-$	$9.8 \pm 0.3$	$4.7 \pm 0.1$	$18.3 \pm 0.4$	$6.4 \pm 0.1$
$R_3^+$	$10.0 \pm 0.4$	$5.1 \pm 0.1$	$15.5 \pm 1.2$	$5.6 \pm 0.2$

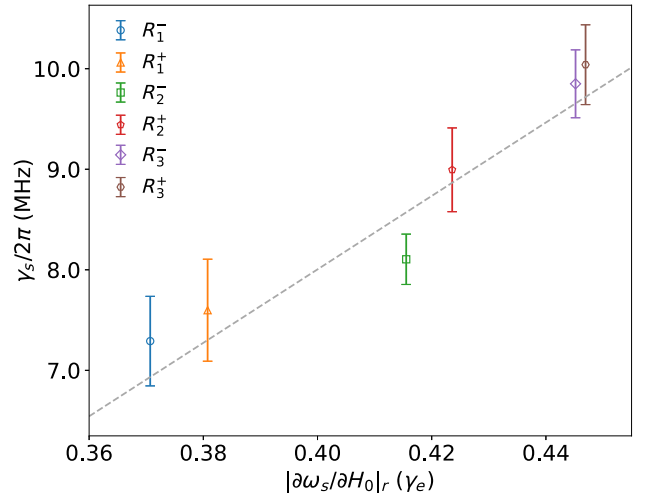


FIG. 5. Spin decoherence rate  $\gamma_s/2\pi$  from cavity width fits versus  $|\partial\omega_s/\partial H_0|_r$ .

The value of decoherence rate  $\gamma_s$  compares well against continuous wave and transient pulse spin echo measurements performed at 6 K [29], which show similar spectral linewidths of 14–42 MHz ( $T_2^* = 25$ –70 ns), while the phase memory times are significantly longer ( $T_2 \approx 5$ –10  $\mu$ s). The nature of the linewidth is inhomogeneous [29] but the long spin-echo time is instrumental in reducing the decoherence effects and the spin sensitivity per  $\sqrt{\text{Hz}}$ . The phase memory loss rate can be attributed to intrinsic mechanisms such as spin-lattice relaxation and dipolar interactions with neighboring Gd or  $^{183}\text{W}$  isotopes and, most importantly, to random distribution of electric field effects on the crystal-field spin Hamiltonian [48]. The  $\text{Gd}^{3+}$  replaces  $\text{Ca}^{2+}$  causing a random distribution of internal charge compensation regions. To fully elucidate the nature of the intrinsic decoherence mechanisms at subkelvin temperatures, spin-echo or Carr-Purcell-Meiboom-Gill pulse sequences are to be explored.

For the given Gd-doped concentration and effective cavity volume a rough estimation of the total number of spins is  $N_{\text{tot}} = 1.78 \times 10^9$  and the number of spins excited per transition is obtained as in Ref. [12],  $N_s = N_{\text{tot}}[0.304/(2I + 1)]\kappa_c/\gamma_s = 7.55 \times 10^7$  spins, where 30.4% is the natural abundance of Gd odd isotopes. In order to estimate the number of spins that contribute to the signal, the spin-photon coupling strengths are calculated for the different mode volumes shown in Fig. 2(c) as detailed in Supplemental Material Sec. II [37]. The numerical analysis, based on COMSOL and EasySpin simulations, reveals that the mode volume is actually well approximated by Eq. (1) and the most important microwave field component is the one  $\perp c$  axis. It is worth noticing that  $N_s$  is of the same order of magnitude as that obtained with sensitive spin detection techniques based on direct current-Superconducting QUantum Interference Device

loops [26,27,49] and other techniques [50,51]. Using an average value of  $g_c/2\pi = 4.2 \pm 0.4$  MHz from cavity width measurements, the average single spin coupling can be estimated as  $g_0/2\pi = g_c/2\pi/\sqrt{N_s} \approx 480 \pm 50$  Hz. In our study,  $N_s$  represents the total number of spins obtained in a continuous-wave experiment (large bandwidth). The spin sensitivity per  $\sqrt{\text{Hz}}$  can be improved by the use of quantum limited parametric amplification combined with the use of advanced pulsed sequences [12,50] and including submicrometer-scale constrictions at the anti-node location as done in the case of *LC* planar microresonators with nanometer-wide inductance strip [52,53].

CaWO<sub>4</sub> is an excellent host for a spin-diluted quantum memory due to its low nuclear magnetic moment density (only <sup>183</sup>W carries  $I = 1/2$  with natural abundance 14%) and thus low spin bath fluctuations. Recently [54], Er<sup>3+</sup> ( $S = 1/2$ ) ions diluted in CaWO<sub>4</sub> demonstrated a 23-ms coherence time measured by a single Hahn echo sequence at millikelvin temperatures using an *LC* resonator patterned directly on the crystal. It is likely that the Gd<sup>3+</sup> ions have larger resonator-spin coupling due to a larger magnetic moment and, at the same time, a larger operating Hilbert space since  $S = 7/2$ .

## V. CONCLUSION

To conclude, we present the coupling of the electromagnetic mode of a superconducting  $\Omega$  loop with the electronuclear states of <sup>155,157</sup>Gd isotopes diluted in a nonmagnetic crystal. Highly sensitive measurements of cavity perturbation in reflected signal make possible the study of forbidden transitions in transverse field. Spin phase memory loss rates and spin-photon coupling constant are obtained for six hyperfine resonance lines. These results present an opportunity for on-chip control of an electronuclear system with close transition frequencies and limited Hilbert space for quantum operations.

## ACKNOWLEDGMENTS

This work was performed at NHMFL at the Florida State University and supported by the National Science Foundation through Grant No. NSF/DMR-1644779 and the State of Florida. We acknowledge discussions with Dr. Petru Andrei (FSU) and we thank Dr. A. M. Tkachuk for providing the sample. S.B. acknowledges support from the CNRS research infrastructure RENARD (award no. IR-RPE CNRS 3443). L.C. acknowledges partial support by the Frontier Science Key Programs and the Young Investigator Program of the CAS (Grants No. QYZDY-SSW-JSC033 and No. 2016217) and the National Natural Science Foundation of China (Grants No. 62071458 and No. 11827805).

- [1] M. Kjaergaard, M. E. Schwartz, J. Braumüller, P. Krantz, J. I. Wang, S. Gustavsson, and W. D. Oliver, Superconducting qubits: Current state of play, *Annu. Rev. Condens. Matter Phys.* **11**, 369 (2020).
- [2] G. Balasubramanian, P. Neumann, D. Twitchen, M. Markham, R. Kolesov, N. Mizuochi, J. Isoya, J. Achard, J. Beck, J. Tissler, V. Jacques, P. R. Hemmer, F. Jelezko, and J. Wrachtrup, Ultralong spin coherence time in isotopically engineered diamond, *Nat. Mater.* **8**, 383 (2009).
- [3] S. Bertaina, H. Vezin, H. De Raedt, and I. Chiorescu, Experimental protection of quantum coherence by using a phase-tunable image drive, *Sci. Rep.* **10**, 1 (2020).
- [4] M. Blencowe, Quantum computing: Quantum RAM, *Nature* **468**, 44 (2010).
- [5] Y. Kubo, C. Grezes, A. Dewes, T. Umeda, J. Isoya, H. Sumiya, N. Morishita, H. Abe, S. Onoda, T. Ohshima, V. Jacques, A. Dréau, J.-F. Roch, I. Diniz, A. Auffeves, D. Vion, D. Esteve, and P. Bertet, Hybrid Quantum Circuit with a Superconducting Qubit Coupled to a Spin Ensemble, *Phys. Rev. Lett.* **107**, 220501 (2011).
- [6] A. Ghirri, C. Bonizzoni, F. Troiani, N. Buccheri, L. Beverina, A. Cassinese, and M. Affronte, Coherently coupling distinct spin ensembles through a high- $T_c$  superconducting resonator, *Phys. Rev. A* **93**, 1 (2016).
- [7] C. Bonizzoni, A. Ghirri, M. Atzori, L. Sorace, R. Sessoli, and M. Affronte, Coherent coupling between vanadyl phthalocyanine spin ensemble and microwave photons: Towards integration of molecular spin qubits into quantum circuits, *Sci. Rep.* **7**, 1 (2017).
- [8] I. Chiorescu, N. Groll, S. Bertaina, T. Mori, and S. Miyashita, Magnetic strong coupling in a spin-photon system and transition to classical regime, *Phys. Rev. B - Condens. Matter Mater. Phys.* **82**, 1 (2010).
- [9] Y. Kubo, F. R. Ong, P. Bertet, D. Vion, V. Jacques, D. Zheng, A. Dréau, J. F. Roch, A. Auffeves, F. Jelezko, J. Wrachtrup, M. F. Barthe, P. Bergonzo, and D. Esteve, Strong Coupling of a Spin Ensemble to a Superconducting Resonator, *Phys. Rev. Lett.* **105**, 1 (2010).
- [10] D. I. Schuster, A. P. Sears, E. Ginossar, L. Dicarlo, L. Frunzio, J. J. L. Morton, H. Wu, G. A. D. Briggs, B. B. Buckley, D. D. Awschalom, and R. J. Schoelkopf, High-Cooperativity Coupling of Electron-Spin Ensembles to Superconducting Cavities, *Phys. Rev. Lett.* **105**, 1 (2010).
- [11] R. Amsüss, C. Koller, T. Nöbauer, S. Putz, S. Rotter, K. Sandner, S. Schneider, M. Schramböck, G. Steinhauser, H. Ritsch, J. Schmiedmayer, and J. Majer, Cavity QED with Magnetically Coupled Collective Spin States, *Phys. Rev. Lett.* **107**, 060502 (2011).
- [12] A. Bienfait, J. J. Pla, Y. Kubo, M. Stern, X. Zhou, C. C. Lo, C. D. Weis, T. Schenkel, M. L. Thewalt, D. Vion, D. Esteve, B. Julsgaard, K. Mølmer, J. J. Morton, and P. Bertet, Reaching the quantum limit of sensitivity in electron spin resonance, *Nat. Nanotechnol.* **11**, 253 (2016).
- [13] J. O'Sullivan, O. W. Kennedy, C. W. Zollitsch, M. Šiménas, C. N. Thomas, L. V. Abdurakhimov, S. Withington, and J. J. Morton, Spin-Resonance Linewidths of Bismuth Donors in Silicon Coupled to Planar Microresonators, *Phys. Rev. Appl.* **14**, 1 (2020).
- [14] P. Bushev, A. K. Feofanov, H. Rotzinger, I. Protopopov, J. H. Cole, C. M. Wilson, G. Fischer, A. Lukashenko, and

- A. V. Ustinov, Ultralow-power spectroscopy of a rare-earth spin ensemble using a superconducting resonator, *Phys. Rev. B - Condens. Matter Mater. Phys.* **84**, 3 (2011).
- [15] S. Probst, H. Rotzinger, S. Wünsch, P. Jung, M. Jerger, M. Siegel, A. V. Ustinov, and P. A. Bushev, Anisotropic Rare-Earth Spin Ensemble Strongly Coupled to a Superconducting Resonator, *Phys. Rev. Lett.* **110**, 1 (2013).
- [16] A. Tkalčec, S. Probst, D. Rieger, H. Rotzinger, S. Wünsch, N. Kukharchyk, A. D. Wieck, M. Siegel, A. V. Ustinov, and P. Bushev, Strong coupling of an  $\text{Er}^{3+}$ -doped  $\text{YAlO}_3$  crystal to a superconducting resonator, *Phys. Rev. B - Condens. Matter Mater. Phys.* **90**, 1 (2014).
- [17] M. D. Jenkins, Y. Duan, B. Diosdado, J. J. García-Ripoll, A. Gaita-Ariño, C. Giménez-Saiz, P. J. Alonso, E. Coronado, and F. Luis, Coherent manipulation of three-qubit states in a molecular single-ion magnet, *Phys. Rev. B* **95**, 064423 (2017).
- [18] S. Bertaina, G. Yue, C.-E. Dutoit, and I. Chiorescu, Forbidden coherent transfer observed between two realizations of quasiharmonic spin systems, *Phys. Rev. B* **96**, 024428 (2017).
- [19] S. Bertaina, L. Chen, N. Groll, J. Van Tol, N. S. Dalal, and I. Chiorescu, Multiphoton Coherent Manipulation in Large-Spin Qubits, *Phys. Rev. Lett.* **102**, 050501 (2009).
- [20] M. Orio, J. K. Bindra, J. van Tol, M. Giorgi, N. S. Dalal, and S. Bertaina, Quantum dynamics of  $\text{Mn}^{2+}$  in dimethylammonium magnesium formate, *J. Chem. Phys.* **154**, 154201 (2021).
- [21] S. Probst, H. Rotzinger, A. V. Ustinov, and P. A. Bushev, Microwave multimode memory with an erbium spin ensemble, *Phys. Rev. B* **92**, 014421 (2015).
- [22] C. Grezes, B. Julsgaard, Y. Kubo, W. L. Ma, M. Stern, A. Bienfait, K. Nakamura, J. Isoya, S. Onoda, T. Ohshima, V. Jacques, D. Vion, D. Esteve, R. B. Liu, K. Mølmer, and P. Bertet, Storage and retrieval of microwave fields at the single-photon level in a spin ensemble, *Phys. Rev. A* **92**, 020301 (2015).
- [23] V. Ranjan, J. O'Sullivan, E. Albertinale, B. Albanese, T. Chanelière, T. Schenkel, D. Vion, D. Esteve, E. Flurin, J. Morton, and P. Bertet, Multimode Storage of Quantum Microwave Fields in Electron Spins over 100 ms, *Phys. Rev. Lett.* **125**, 210505 (2020).
- [24] S. Probst, N. Kukharchyk, H. Rotzinger, A. Tkalčec, S. Wünsch, A. D. Wieck, M. Siegel, A. V. Ustinov, and P. A. Bushev, Hybrid quantum circuit with implanted erbium ions, *Appl. Phys. Lett.* **105**, 162404 (2014).
- [25] I. Wisby, S. E. de Graaf, R. Gwilliam, A. Adamyan, S. E. Kubatkin, P. J. Meeson, A. Y. Tzalenchuk, and T. Lindström, Coupling of a locally implanted rare-earth ion ensemble to a superconducting micro-resonator, *Appl. Phys. Lett.* **105**, 102601 (2014).
- [26] G. Yue, L. Chen, J. Barreda, V. Bevara, L. Hu, L. Wu, Z. Wang, P. Andrei, S. Bertaina, and I. Chiorescu, Sensitive spin detection using an on-chip SQUID-waveguide resonator, *Appl. Phys. Lett.* **111**, 202601 (2017).
- [27] R. P. Budoyo, K. Kakuyanagi, H. Toida, Y. Matsuzaki, W. J. Munro, H. Yamaguchi, and S. Saito, Electron paramagnetic resonance spectroscopy of  $\text{Er}^{3+}:\text{Y}_2\text{SiO}_5$  using a Josephson bifurcation amplifier: Observation of hyperfine and quadrupole structures, *Phys. Rev. Mater.* **2**, 1 (2018).
- [28] S. Bertaina, S. Gambarelli, A. Tkachuk, I. N. Kurkin, B. Malkin, A. Stepanov, and B. Barbara, Rare-earth solid-state qubits, *Nat. Nanotechnol.* **2**, 39 (2007).
- [29] E. I. Baibekov, M. R. Gafurov, D. G. Zverev, I. N. Kurkin, A. A. Rodionov, B. Z. Malkin, and B. Barbara, Coherent spin dynamics in a gadolinium-doped  $\text{CaW O}_4$  crystal, *Phys. Rev. B* **95**, 1 (2017).
- [30] M. N. Leuenberger and D. Loss, Quantum computing in molecular magnets, *Nature* **410**, 789 (2001).
- [31] N. Groll, A. Gurevich, and I. Chiorescu, Measurement of the nonlinear Meissner effect in superconducting Nb films using a resonant microwave cavity: A probe of unconventional pairing symmetries, *Phys. Rev. B - Condens. Matter Mater. Phys.* **81**, 1 (2010).
- [32] S. Kwon, A. Fadavi Roudsari, O. W. Benningshof, Y. C. Tang, H. R. Mohebbi, I. A. Taminiou, D. Langenberg, S. Lee, G. Nichols, D. G. Cory, and G. X. Miao, Magnetic field dependent microwave losses in superconducting niobium microstrip resonators, *J. Appl. Phys.* **124**, 033903 (2018).
- [33] J. G. Kroll, F. Borsoi, K. L. Van Der Enden, W. Uilhoorn, D. De Jong, M. Quintero-Pérez, D. J. Van Woerkom, A. Bruno, S. R. Plissard, D. Car, E. P. Bakkers, M. C. Cassidy, and L. P. Kouwenhoven, Magnetic-Field-Resilient Superconducting Coplanar-Waveguide Resonators for Hybrid Circuit Quantum Electrodynamics Experiments, *Phys. Rev. Appl.* **11**, 1 (2019).
- [34] D. E. Anagnostou, M. Morton, J. Papapolymerou, and C. G. Christodoulou, A 0–55-GHz coplanar waveguide to coplanar strip transition, *IEEE Trans. Microw. Theory Tech.* **56**, 1 (2008).
- [35] G. Agrawal, in *Nonlinear Fiber Optics (Fifth Edition)*, Optics and Photonics, edited by G. Agrawal (Academic Press, Boston, 2013) fifth edition ed., p. 34.
- [36] Calculating the modal volume of a cavity mode, <https://support.lumerical.com/hc/en-us/articles/360034395374-Calculating-the-modal-volume-of-a-cavity-mode>.
- [37] G. Franco-Rivera, J. Cochran, L. Chen, S. Bertaina, and I. Chiorescu, See Supplemental Material at <http://link.aps.org/supplemental/10.1103/PhysRevApplied.18.014054> for details of the fitting procedure and coupling strength estimation.
- [38] A. Zalkin and D. H. Templeton, X-ray diffraction refinement of the calcium tungstate structure, *J. Chem. Phys.* **40**, 501 (1964).
- [39] C. F. Hempstead and K. D. Bowers, Paramagnetic resonance of impurities in  $\text{CaWO}_4$ . I. Two S-state ions, *Phys. Rev.* **118**, 131 (1960).
- [40] C. Rudowicz and C. Y. Chung, The generalization of the extended Stevens operators to higher ranks and spins, and a systematic review of the tables of the tensor operators and their matrix elements, *J. Phys. Condens. Matter* **16**, 5825 (2004).
- [41] J. S. M. Harvey and H. Kiefte, Temperature dependence of the crystal-field splittings in  $\text{Gd}^{3+}:\text{CaWO}_4$ , *Can. J. Phys.* **49**, 995 (1971).
- [42] S. K. Yip and J. A. Sauls, Nonlinear Meissner Effect in CuO Superconductors, *Phys. Rev. Lett.* **69**, 2264 (1992).
- [43] S. Donovan, O. Klein, M. Dressel, K. Holczer, and G. Grüner, Microwave cavity perturbation technique: Part II: Experimental scheme, *Int. J. Infrared Millimeter Waves* **14**, 2459 (1993).

- [44] P. F. Herskind, A. Dantan, J. P. Marler, M. Albert, and M. Drewsen, Realization of collective strong coupling with ion Coulomb crystals in an optical cavity, *Nat. Phys.* **5**, 494 (2009).
- [45] E. Abe, H. Wu, A. Ardavan, and J. J. Morton, Electron spin ensemble strongly coupled to a three-dimensional microwave cavity, *Appl. Phys. Lett.* **98**, 251108 (2011).
- [46] A. Angerer, T. Astner, D. Wirtitsch, H. Sumiya, S. Onoda, J. Isoya, S. Putz, and J. Majer, Collective strong coupling with homogeneous Rabi frequencies using a 3D lumped element microwave resonator, *Appl. Phys. Lett.* **109**, 033508 (2016).
- [47] S. Stoll and A. Schweiger, EasySpin, a comprehensive software package for spectral simulation and analysis in EPR, *J. Magn. Reson.* **178**, 42 (2006).
- [48] E. I. Baibekov and I. N. Kurkin, Inhomogeneous broadening of ESR lines of rare earth impurities in scheelite  $\text{CaWO}_4$  induced by internal electric field gradients, *J. Phys.: Conf. Ser.* **324**, 012009 (2011).
- [49] H. Toida, Y. Matsuzaki, K. Kakuyanagi, X. Zhu, W. J. Munro, K. Nemoto, H. Yamaguchi, and S. Saito, Electron paramagnetic resonance spectroscopy using a direct current-squid magnetometer directly coupled to an electron spin ensemble, *Appl. Phys. Lett.* **108**, 052601 (2016).
- [50] C. Eichler, A. J. Sigillito, S. A. Lyon, and J. R. Petta, Electron Spin Resonance at the Level of 104 Spins Using Low Impedance Superconducting Resonators, *Phys. Rev. Lett.* **118**, 1 (2017).
- [51] S. Weichselbaumer, P. Natzkin, C. W. Zollitsch, M. Weiler, R. Gross, and H. Huebl, Quantitative Modeling of Superconducting Planar Resonators for Electron Spin Resonance, *Phys. Rev. Appl.* **12**, 024021 (2019).
- [52] S. Probst, A. Bienfait, P. Campagne-Ibarcq, J. J. Pla, B. Albanese, J. F. Da Silva Barbosa, T. Schenkel, D. Vion, D. Esteve, K. Mølmer, J. J. Morton, R. Heeres, and P. Bertet, Inductive-detection electron-spin resonance spectroscopy with 65 spins/ $\sqrt{\text{Hz}}$  sensitivity, *Appl. Phys. Lett.* **111**, 202604 (2017).
- [53] V. Ranjan, S. Probst, B. Albanese, T. Schenkel, D. Vion, D. Esteve, J. J. Morton, and P. Bertet, Electron spin resonance spectroscopy with femtoliter detection volume, *Appl. Phys. Lett.* **116**, 1 (2020).
- [54] M. Le Dantec, M. Rančić, S. Lin, E. Billaud, V. Ranjan, D. Flanigan, S. Bertaina, T. Chanelière, P. Goldner, A. Erb, R. B. Liu, D. Estève, D. Vion, E. Flurin, and P. Bertet, Twenty-three-millisecond electron spin coherence of erbium ions in a natural-abundance crystal, *Sci. Adv.* **7**, eabj9786 (2021).